Received 12 October 2016; revised 14 November 2016; accepted 22 November 2016. Date of publication 24 November 2016; date of current version 20 December 2016. The review of this paper was arranged by Editor M. Sangiorgi.

Digital Object Identifier 10.1109/JEDS.2016.2632709

A Continuous Compact DC Model for Dual-Independent-Gate FinFETs

MEHDI HASAN, PIERRE-EMMANUEL GAILLARDON (Member, IEEE), AND BERARDI SENSALE-RODRIGUEZ (Member, IEEE)

Department of Electrical and Computer Engineering, University of Utah, Salt Lake City, UT 841112, USA

CORRESPONDING AUTHOR: B. SENSALE-RODRIGUEZ (email: berardi.sensale@utah.edu)

This work was supported by the NSF under Award ECCS-1407959 and Award EAGER-1644592.

ABSTRACT Multiple-independent-gate (MIG) silicon FinFETs were recently shown capable of enabling: 1) device-level polarity control; 2) dynamic threshold modulation; and 3) subthreshold slope tuning down to ultra-steep-slope operation. These operation mechanisms can unlock a myriad of opportunities in digital as well as analog design. Here we discuss a continuous compact direct-current (dc) model, capable of describing the current–voltage characteristics of a class of MIG FinFETS, namely dual-independent-gate (DIG) FinFETs, over all its biasing design space. This model captures some of the unique features of DIG FinFETs including the dependence of its super-steep subthreshold swing on drain bias and polarity gate bias. An excellent agreement is shown between the model and measured experimental current–voltage characteristics in these devices. Moreover, the predictive nature of the model is evaluated by foreseeing the perspectives of DIG FinFETs as efficient RF detectors at very high frequencies.

INDEX TERMS Compact model, FinFET, Schottky barrier, steep subthreshold slope, impact ionization, feedback.

I. INTRODUCTION

In order to reduce the power consumption in digital integrated circuits, increase the trans-conductance generation efficiency (g_m/I_D) of transistors in analog circuits, and for attaining a very sensitive nonlinear response to radio-frequency, transistors attaining very steep subthreshold slope (*SS*) at room-temperature are required. The subthreshold slope in conventional MOSFETs is limited to > 60 mV/dec due to the turn-on mechanism for current in such devices being thermionic emission. To overcome this fundamental limit, different types of field-effect transistors, based on alternative current mechanisms, have been proposed during the last decade. In this regard, Tunnel FETs (TFETs) [1]–[5], in which the current turn-on mechanism is band-to-band tunneling rather than thermionic emission, have emerged as an attractive alternative to traditional MOSFETs. Experimental demonstration of such devices showing *SS* below 30 mV/dec over four decades of current has been recently reported [4]. In addition to TFETs, Dual-Independent-Gate (DIG) FinFETs [6], [7] have been also recently demonstrated capable of achieving a very steep subthreshold slope ($SS << 60$ mV/dec at room-temperature). The reason behind this super steep slope is a positive feedback induced by carrier multiplication due to weak impact ionization under proper biasing conditions [6]–[10]. In this regard, experimental demonstrations of DIG FinFETs have shown *SS* as small as 3.4 mV/dec at room-temperature and the possibility of attaining such small slopes over five decades of current swing [6], [10].

In order to design circuits based on DIG FinFETs and to evaluate and project the performance of these devices for analog and RF applications, it is of interest to develop a simple, closed form, continuous analytical model for its current-voltage characteristics. *This model must: (i) contain the basic physics of weak impact ionization during the ON-transition, and, also, (ii) be capable of capturing the dependence of the current on the voltages applied at all four-terminals of the device*. Here, we report for the first time on a simple and continuous model capable of describing the current-voltage characteristics of DIG FinFETs in all its operation regions. Moreover, the proposed model is capable of capturing all the essential features observed in this device.

2168-6734 © 2016 IEEE. Translations and content mining are permitted for academic research only.
Personal use is also permitted, but republication/redistribution requires IEEE permission.
See http://www.ieee.org/publications_standards/publications/rights/index.html for more information.

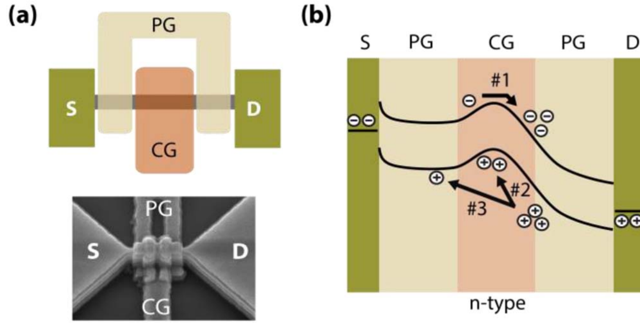

FIGURE 1. (a) Structure sketch and SEM images of fabricated DIG FinFET, and (b) conceptual band diagram for an *n*-type device illustrating the mechanism of impact-ionization during the ON-transition. Figure adapted from [6].

From the measured *I-V* characteristics of fabricated devices previously reported in [6], we find a set of parameters that enable an excellent fit between the experimental data and the proposed continuous compact model. Moreover, besides enabling circuit design, we discuss how the proposed model can also predict potential future applications of these devices, for instance as efficient RF detectors.

The remainder of this paper is organized as follows. Section II describes the operation of DIG FinFETS. Section III introduces a compact, continuous, model, and describes its peculiarities. Experimental data is fitted to this model showing an excellent agreement. Finally, Section IV discusses the predictive nature and applications of the proposed model.

II. OPERATION OF DIG FINFETS

A sketch of the structure and a SEM image of a DIG FinFET are depicted in Fig. 1a. The device consists of a fin-shaped silicon channel, metallic source and drain contacts, and two independent gate electrodes. In general, in multiple-independent-gate (MIG) FinFETs, there are two polarity gates, a source-polarity gate (PG_S) and a drain-polarity gate (PG_D), which modulate the Schottky barriers at the source and drain ends of the device. Moreover, a control gate (CG) controls the potential barrier in the channel and thus can govern whether the device is in ON or OFF state. In DIG FinFETs, the PG_D and PG_S terminals are electrically connected, thus leading to a single polarity gate (PG), as depicted in Fig. 1(a) [6], [7]. The device depicted in Fig. 1(a), which will be discussed herein, has a channel length of ∼600 nm (CG length 200 nm); the fin height and width are 340 nm and ∼60 nm, respectively [6]. Although fit of experimental data to the proposed model will be performed at the 200 nm CG node, results from numerical simulations employing TCAD Sentaurus predict the validity of the model for shorter channel devices (e.g., 50 nm). Control of carrier injection at the Schottky barrier by the polarity gate, offers the possibility of arbitrarily setting the operation mode of the device as either *n*-type or *p*-type [6], [7]. The polarity gate tunes the Schottky barriers at the source/drain junctions, therefore selecting the type of majority charge carriers injected in the channel. Although the discussion in this manuscript will be focus on the quadrant where *n*-type operation is achieved, the same functional model, although employing a different set of parameters, could be employed in the quadrant where the device exhibits *p*-type operation.

Depicted in Fig. 1b is the operation mechanism of the device. Application of a positive voltage on the polarity gate creates a potential well under this terminal. When a voltage is applied on the control gate, at the onset of conduction, conducting electrons can acquire enough energy so that electron-hole pairs are generated by impact ionization as indicated by step #1 in Fig. 1b. The electrons drift towards the drain and the generated holes accumulate in the potential well under the control gate as indicted by step #2 in Fig. 1b. This lowers the potential barrier and provides for further electrons for impact ionization. In this process, the more electron-hole pairs that are generated, the lower the potential barrier becomes, thus setting a positive feedback. Another factor that further enhances this carrier multiplication process is modulation of the Schottky barrier by the holes that are swept towards the source, as depicted in step #3 in Fig. 1b. Because of this positive feedback, very steep subthreshold slope ($SS << 60\,\mathrm{mV/dec}$) is possible in DIG FinFETs.

III. MODEL

To physically understand the steep subthreshold in the DIG FinFET *I-V* characteristics, it is worth noticing that the impact ionization current can be mathematically expressed by [7] and [8]:

$$I(V_{GS}) = I_0 e^{\frac{qV_{GS}}{nkT}}, \tag{1}$$

where:

$$n = (1+r)/\left(1 + r\frac{dV_{BS}}{dV_{GS}}\right), \tag{2}$$

and, $r = \frac{2\epsilon_{Si} t_{ox}}{\epsilon_{ox} t_{Si}}$. Here, q is the electron charge, k is Boltzmann's constant, T is temperature; t_{ox} is the thickness of the oxide layer and t_{si} is the width of the fin, ε_{ox} and ε_{si}, are the permittivities of the oxide layer and Si, respectively. Moreover, V_{BS} is the difference between $V_{B,CG}$ and the voltage at the source terminal (V_S), where the potential $V_{B,CG}$ is the potential at the middle point between the two sidewalls of the fin in the gate-controlled region. *When the carriers generated by impact ionization charge the body, it is possible to have $dV_{BS}/dV_{GS} > 1$, and thus n smaller than unity; which leads to $SS < 60\ mV/dec$.*

As discussed in [7] and [8], dV_{BS}/dV_{GS} is given by the following (approximate) expression:

$$\frac{dV_{BS}}{dV_{GS}} \approx \frac{m}{n}\frac{1}{1 + I_{gt}/I_{gi}} \propto \frac{m}{n} e^{\left[\frac{q}{kT}\left(\frac{V_{GS}}{n} - \frac{V_{B,CG} - V_{B,\ PGS}}{m}\right)\right]} \cdot e^{-\frac{\beta_i l}{V_{DS}}}, \tag{3}$$

where $V_{B,PGS}$ is the center potential in the source polarity gate region, m is an ideality factor in the junction between the region controlled by the control gate and the region controlled by the source-end of the polarity gate, I_{gt} is the *off*-state leakage current, and I_{gi} is the impact ionization current [7]. Furthermore, in Eqn. (3), β_i is a constant and l is a structural parameter.

In our model, so to properly represent the device characteristics across all bias operation regions, the current voltage characteristics of the DIG FinFET will be expressed by:

$$I = C_T f_{IIF} V_{LF}, \tag{4}$$

where: (*i*) f_{IIF} is a dimensionless, bias dependent, factor capable of capturing the steep subthreshold slope in the device, and also capable of smoothly connecting the subthreshold and the above-threshold regions of operation. And, (*ii*) V_{LF} is a bias-dependent term that mainly captures the device behavior above threshold. Moreover, (*iii*) C_T is a factor that sets the current levels thus is dependent on the Drain-Source (DS) bias as well as the polarity gate (PG) bias. Equation (4) is employed in analogy to the compact analytical model developed for steep-slope TFETs in [11]–[16]. Although the physical mechanisms behind the steep current turn-on mechanism in TFETs and DIG FinFETs are intrinsically different, the functional dependences for current on V_{GS} during the onset of conduction are rather similar. In both devices the subthreshold current depends exponentially on V_{GS} and the associated SS can be $<<$ 60 mV/dec. In this regard, it is worth mentioning that in [11] and [12] the authors developed a similar compact model for the *I-V* characteristics of TFETs based on analyzing the device operation in each region of operation and extending the equations ruling the device response in each region to be continuous across all regions of operation.

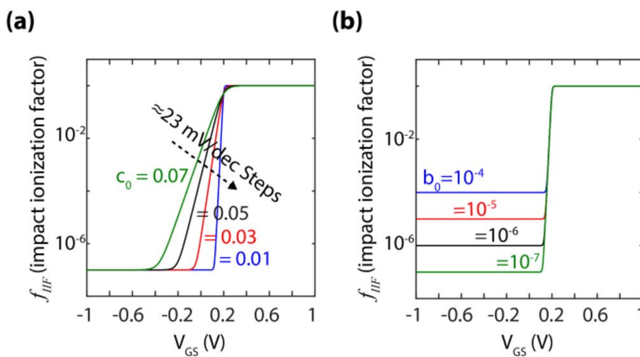

FIGURE 2. **Impact ionization factor (f_{IIF}) as a function of V_{GS} for: (a) c_0 ranging from 10mV to 70mV in 20mV steps (corresponds to variations in SS of approx. 23mV/dec per curve), and $b_0 = 10^{-7}$, thus 7 decades variation in drain current; and (b) b_0 ranging from 10^{-4} to 10^{-7}, and $c_0 =$ 10mV. In both plots $V_{OFF} = 0.2$V is employed.**

A. SUBTHRESHOLD REGION

A characteristic signature of DIG FinFETs is the possibility of attaining (at proper V_{DS} and V_{PG} biases) a very steep subthreshold slope, which, as previously discussed, arises from impact ionization processes during the ON-transition. When the bias voltage becomes much smaller than the threshold voltage, experimental results evidence the presence of a constant (i.e., V_{GS} independent) leakage current. In order to accurately depict the operation of the device in the subthreshold regime, a compact model should be able to capture the following two effects, namely: (a) leakage current (current level at OFF-state), and (b) steep subthreshold slope at the onset of ON-state, which is dictated by an exponential dependence on V_{GS} as per Eqn. (1). These two features are simultaneously captured in our model by considering an impact ionization factor, which is given by:

$$f_{IIF} = \left\{ \frac{1}{2} + \left(\frac{1}{2} - b_0 \right) \ tanh \left(\frac{V_{GS} + V_{OFF}}{c_0} \right) \right\}, \tag{5}$$

where: (*i*) b_0 is a factor setting the ON/OFF current ratio, (*ii*) c_0 is a fitting parameter, which sets the subthreshold slope, and (*iii*) V_{OFF} is an offset voltage. Depicted in Fig. 2a is the dependence of f_{IIF} on c_0 (for a fixed V_{OFF} and b_0). It is important to mention, that besides being capable of capturing the OFF-state behavior and subthreshold slope, because of the asymptotic limit of hyperbolic tangent to one, f_{IIF} also works as a smoothing function capable of efficiently connecting the subthreshold and above-threshold regions. The dependence of f_{IIF} on b_0 is analyzed in Fig. 2b, where c_0 was fixed to $c_0 =$ 10 mV, which corresponds to a ~12 mV/dec subthreshold slope. Since experimental data on DIG FinFETs shows constant, steep, slopes over multiple decades of current swing [6], and due to the fact that in Eqn. (5) b_0 constitutes a factor related to the minimum attainable value by f_{IIF} (i.e., it can be noticed that f_{IIF} ranges between 1 - b_0 and b_0 at its asymptotic limits on V_{GS}), b_0 will usually be a "small number," i.e., $b_0 << 1$ thus the upper bound of f_{IIF} approaches one. Typical values of b_0, ranging from 10^{-4} to 10^{-7}, are used in order to show the dependence of f_{IIF} on b_0, which is depicted in Fig. 2(b). As can be noticed in Fig. 2(b), besides being related to the ON/OFF current ratio, b_0 is also related to the current swing over which maximum SS is observed. These observations are useful for understanding how these parameters are related to the current-voltage characteristics of the device, and for later exploring functional forms for their dependences on V_{DS} and V_{PG}. Finally, it is also worth mentioning that this model can be adapted to describe the p-type operation of DIG FinFETs simply by just changing the sign of the parameter c_0.

B. ABOVE-THRESHOLD REGION

The region above threshold is modeled employing a functional dependence of the form:

$$V_{LF} = \begin{cases} b_1 (V_{GS} + V_{OFF})^{c_1} + 1; & V_{GS} + V_{OFF} > 0 \\ 1; & otherwise \end{cases}, \tag{6}$$

where: c_1 and b_1 are fitting parameters setting the order and strength of the current voltage dependence, and V_{OFF} is an offset voltage. Based on experimental data (see Section III-D), we observe that in general $1 < c_1 < 2$,

thus *although piecewise defined, V_{LF} results continuous and its derivative is also continuous*. The dependence of V_{LF} on b_1 and c_1 is shown in Fig. 3a and Fig. 3b, respectively. By tuning these two parameters (b_1 and c_1) simultaneously, the properties of the device in the region above threshold can be well represented, as will be discussed in Section III-D, by means of fitting the model to experimental data.

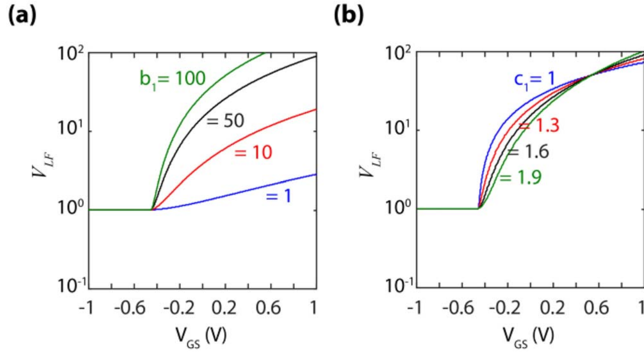

FIGURE 3. V_{LF} function plotted (a) for varying b_1 with $c_1 = 1.6$; and (b) for varying c_1 from 1 to 1.9 in steps of 0.3 with $b_1 = 50$; according to Eqn. (6), for both plots $V_{OFF} = 0.45$ is employed.

C. I_{DS}-V_{GS} MODEL

After applying the definitions for f_{IIF} and V_{LF} given in Eqn. (5) and Eqn. (6), the complete current equation for the DIG FinFET becomes of the form:

$$I(V_{GS}) = C_T \left[b_1 (V_{GS} + V_{OFF})^{c_1} H(V_{GS}, V_{OFF}) + 1 \right] \cdot \times \left[\frac{1}{2} + \left(\frac{1}{2} - b_0 \right) tanh \left(\frac{V_{GS} + V_{OFF}}{c_0} \right) \right]. \quad (7)$$

where $H(V_{GS}, V_{OFF})$ is the Heaviside step function evaluated at $V_{GS} - V_{OFF}$. A typical plot of current as a function of V_{GS} (assuming $C_T = 1$) is shown in Fig. 4 together with the correspondent plots of f_{IIF} and V_{LF} leading to it. We observe, in general, that choosing the same values for the offset voltages in f_{IIF} and V_{LF} qualitatively produces a very smooth transition betwen both bias regimes. In the following discussion we will assume this condition.

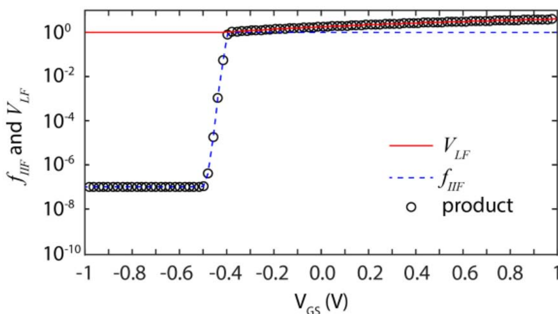

FIGURE 4. f_{IIF}, V_{LF}, and their product, as a function of the control gate voltage (V_{GS}). The parameters employed in this calculation are: $b_0 = 10^{-7}$, $c_0 = 10\,mV$, $V_{OFF} = 0.4V$, $b_1 = 2$, $c_1 = 1.1$.

D. DEPENDENCE ON V_{DS} AND V_{PG}

In order to provide for a complete compact model, the current dependences on V_{DS} and V_{PG} should be analyzed from this point of view, and, in accordance with Eqn. (7), we will model for the dependences of the unknown parameters, i.e., b_0, c_0, b_1, c_1, V_{OFF}, and C_T, on these voltages. Of these parameters, the parameters that have a more clear physical meaning, and which will be discussed in most depth are b_0 and c_0, which are directly related to the ON/OFF current ratio and SS.

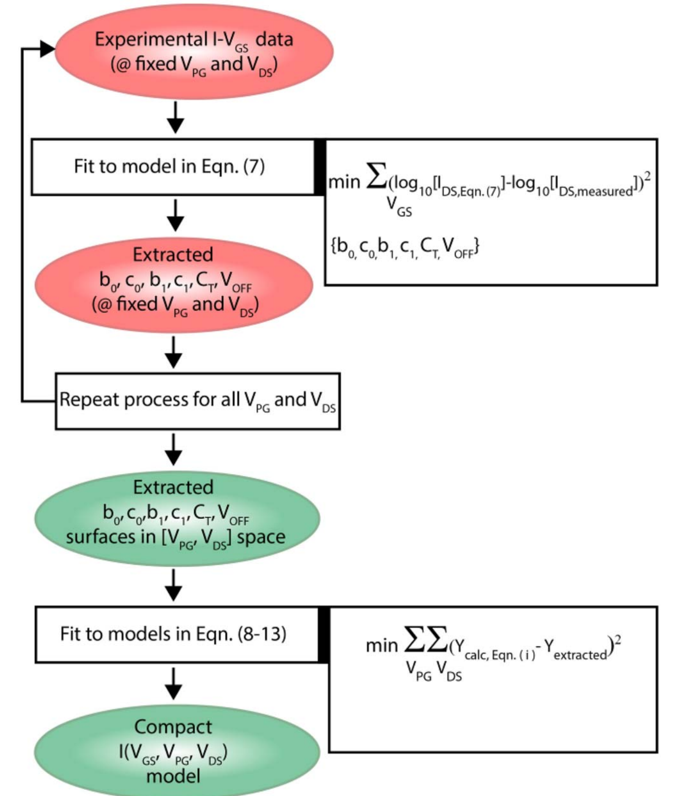

FIGURE 5. Flow chart of the procedure employed to determine the model parameters.

In accordance with Eqns. (2) and (3) it is observed that n decreases exponentially with V_{DS} and V_{PG}. From Eqn. (2) and (3), the following expression can be derived for the mathematical dependence of c_0 on V_{DS} and V_{PG}:

$$c_0 = \frac{\alpha_0}{\left(1 + \beta_0 e^{\gamma_0 V_{PG}} e^{\delta_0 V_{DS}}\right)}, \quad (8)$$

where α_0, β_0, γ_0, and δ_0 are constants. By means of determining c_0 at different values of V_{DS} and V_{PG} via fitting the measured $I_{DS} - V_{GS}$ to the model in Eqn. (7), the values of these unknown constants can be extracted. Similar procedures will be employed to find the voltage dependences of the other five parameters in Eqn. (7). Depicted in Fig. 5 is a sketch of the procedure employed so to extract the complete voltage dependences for all the model parameters. More details about the parameter extraction will be discussed in the next subsection.

E. PARAMETER EXTRACTION

We extracted the $b_0, c_0, b_1, c_1, C_T, V_{OFF}$ from the measured $I_{DS} - V_{GS}$ characteristics at different values of V_{PG} and V_{DS} by means of fitting experimental data to the model in Eqn. (4). The extracted parameters were found by using the Nonlinear Least Squares Error method (NLSE) [17] to minimize the following error function:

$$e_0\left(b_0, c_0, b_1, c_1, C_T,\ V_{OFF}\right) = \sum_{V_{GS}=-1V}^{V_{GS}=1V} \left\{log_{10}\left(I_{DS,Eqn(7)}\right) - log_{10}\left(I_{DS,measured}\right)\right\}^2,$$

where, $I_{DS,Eqn.(7)}$ is the calculated current using Eqn. (7), for a fixed V_{DS} and V_{PG}, and $I_{DS,measured}$ is the measured value for the current. Defining: $Y_1(V_{DS}, V_{PG}) = b_0(V_{DS}, V_{PG})$, $Y_2(V_{DS}, V_{PG}) = c_0(V_{DS}, V_{PG})$, $Y_3(V_{DS}, V_{PG}) = b_1(V_{DS}, V_{PG})$, $Y_4(V_{DS}, V_{PG}) = c_1(V_{DS}, V_{PG})$, $Y_5(V_{DS},\ V_{PG}) = C_T(V_{DS}, V_{PG})$, and $Y_6(V_{DS},\ V_{PG}) = V_{OFF}(V_{DS}, V_{PG})$, 3D plots in the $[V_{DS}, V_{PG}]$ space were then generated for these six functions (Y_i, $i = 1, \ldots 6$). From these 3D plots, the values for the unknown parameters in the Y_i functions were found by means of fitting the extracted values to the mathematical expressions in Eqns. (8)-(13). Fitting was performed via employing a non nonlinear least squares error method to minimize the following error functions:

$$e_i = \sum_{VDS}\sum_{VPG}\left\{Y_{i,calc,Eqn.(n)} - Y_{i,extracted}\right\}^2,$$

where $Y_{i,calc,Eqn.(n)}$ are the calculated values for the Y_i functions at various V_{DS} and V_{PG} using Eqns. (8)-(13) and $Y_{i,extracted}$ are the extracted values.

Depicted in Fig. 6 are the extracted values of c_0 versus V_{PG} (Fig. 6(a)) and V_{DS} (Fig. 6(b)) together with the curves obtained from the best fit of this data to the model in Eqn. (8). Overall, a good qualitative agreement is observed between the physical model in Eqn. (8) and the extracted values of c_0 obtained from fitting the measured device data to the model in Eqn. (7).

At this end, we proceeded to plot the extracted values of b_0 versus V_{PG} (Fig. 7(a)) and V_{DS} (Fig. 7(b)). It is observed that these extracted values, in logarithmic scale, show a linear dependence with V_{PG} as well as V_{DS}. Moreover, b_0 increases with V_{DS}, and decreases with V_{PG}. As discussed in Fig. 2, a smaller b_0 is an indication of a smaller leakage current floor thus a larger ON/OFF current ratio. The fact that b_0 increases with V_{DS} is an evidence of Drain-Induced Barrier Lowering (DIBL) effect [18], which leads to an increased OFF-current leakage current floor as V_{DS} is increased. In contrast, the lower b_0 at larger V_{PG} is a result of a better conduction through the polarity-gate controlled regions, i.e., higher polarity-gate induced doping, which physically translates into a larger ON-current level. Based on the above observations, we employed a model of the form:

$$b_0 = \alpha_1 e^{\beta_1 V_{DS}+\beta_2 V_{PG}+\beta_3 V_{DS}V_{PG}+\beta_4}, \tag{9}$$

in order to model the V_{DS} and V_{PG} dependences in b_0. Depicted in Fig. 7(a)-(b) are the curves obtained from fitting the extracted values of b_0 to the model in Eqn. (9). A good qualitative agreement is observed between the model in Eqn. (9) and the extracted values of b_0 obtained from fitting the measured device data to the model in Eqn. (7).

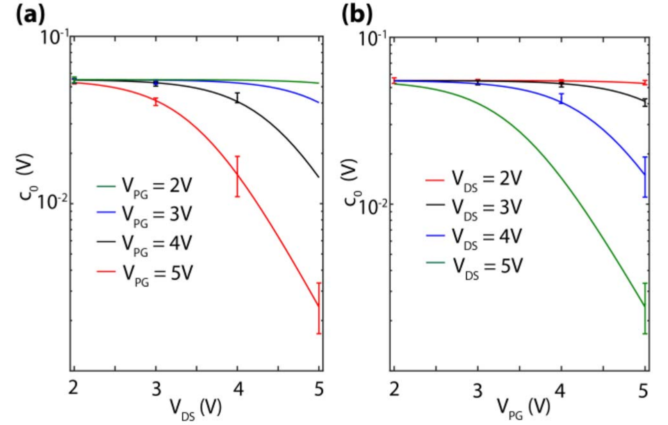

FIGURE 6. Extracted and fitting of c_0 versus (a) V_{PG}, and (b) V_{DS}. Fitting was performed employing the model in Eqn. (8).

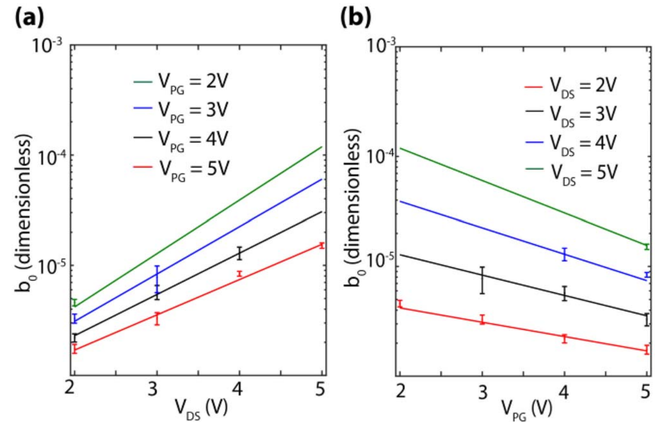

FIGURE 7. Extracted and fitting of b_0 versus (a) V_{PG}, and (b) V_{DS}. Fitting was performed employing the model in Eqn. (9).

In addition, we proceeded to find models for b_1, c_1, C_T, and V_{OFF}. For this purpose we looked at the 3D plots of these parameters in the $[V_{DS}, V_{PG}]$ space and determine adequate functions for fitting these points with a continuous surface. Since the physical origin of these parameters is less clear than that for b_0 and c_0, we employed two-variable polynomials and exponential functions in our fitting models. In this regard, for b_1 and c_1 we will employ a 3rd and 2nd order quadratic equations, respectively, of the form:

$$b_1 = p_0 + p_1 V_{DS} + p_2 V_{PG} + p_3 V_{DS}^2 + p_4 V_{DS}V_{PG} + p_5 V_{PG}^2 + p_6 V_{DS}^3 + p_7 V_{DS}^2 V_{PG} + p_8 V_{DS} V_{PG}^2 + p_9 V_{PG}^3, \tag{10}$$

$$c_1 = q_0 + q_1 V_{DS} + q_2 V_{PG} + q_3 V_{DS}V_{PG} + q_4 V_{PG}^2 + q_5 V_{DS}^2, \tag{11}$$

Moreover, for C_T we will employ a combination of a linear dependence on V_{PG} and an exponential dependence on V_{DS} and V_{PG}, according to the following equation:

$$C_T = \mu_0 + \mu_1 V_{PG} + \mu_2\ e^{\sigma_0 V_{PG} + \sigma_1 V_{DS} + \sigma_2 V_{PG} V_{DS}}, \quad (12)$$

And, for V_{OFF} we will employ polynomial dependences on V_{PG} as well as on V_{DS} of the form:

$$V_{OFF} = r_0 + r_1 V_{DS} + r_2 V_{PG} + r_3 V_{DS}^2 + r_4 V_{DS} V_{PG} + r_5 V_{PG}^2 + r_6 V_{DS}^3 + r_7 V_{DS}^2 V_{PG} + r_8 V_{DS} V_{PG}^2 + r_9 V_{PG}^3. \quad (13)$$

Depicted in Fig. 8 are 3D plots of the extracted values of b_1 (Fig. 8(a)), c_1 (Fig. 8(b)), C_T (Fig. 8(c)), and V_{OFF} (Fig. 8(d)), versus V_{PG} and V_{DS}, together with the surface plots obtained from fitting these extracted values to the models in Eqns. (10)-(13). A good qualitative agreement is observed between these models and the extracted values of the parameters obtained from fitting the measured device data to the model in Eqn. (7).

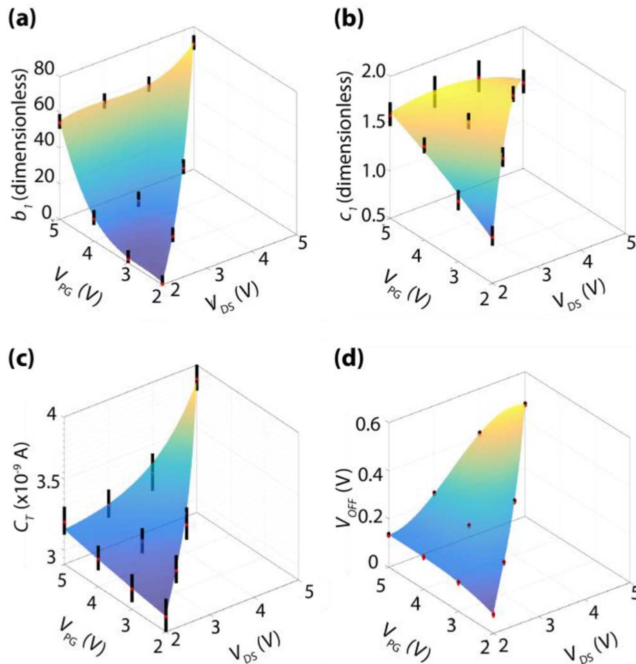

FIGURE 8. 3D plots of the extracted values of: (a) b_1, (b) c_1, (c) C_T, and (d) V_{OFF}, versus V_{PG} and V_{DS}, together with the surfaces fitting these parameters to the models in Eqns. (10)-(13).

Depicted in Fig. 9 are examples of the measured current-voltage characteristics for the analyzed DIG-FinFET, whose performance was reported in [6], together with the calculated current-voltage characteristics obtained via fitting to the continuous compact model here discussed in semi-logarithmic (Fig. 9(a)-(b)) and linear scales (Fig. 9(c)-(d)), showing a good agreement between the model and measurements.

F. I_{DS}-V_{DS} MODEL

Our discussion so far has been focused on the device operating in "saturation" region and on the $I_{DS} - V_{GS}$ characteristics. When analyzing the device characteristics on the V_{DS} domain, it is observed that "saturation" occurs for $V_{DS} > 2$V. Otherwise, when $V_{DS} < 2$V, the current was found to follow a dependence on V_{DS} of the form:

$$I \propto \left(1 - e^{-\frac{V_{DS}{}^B}{A}}\right). \quad (14)$$

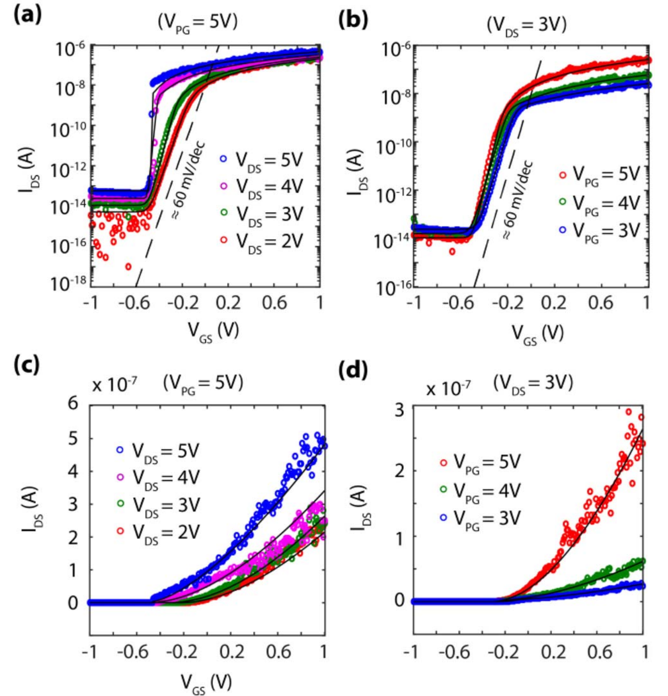

FIGURE 9. Experimental (circles) and modeled $I - V_{GS}$ characteristic for a DIG FinFET. (a) $V_{PG} = 5$V and $V_{DS} = 2, 3, 4, 5$V (logarithmic-scale). (b) $V_{DS} = 3$V and $V_{PG} = 3, 4, 5$V (logarithmic-scale). (c) $V_{PG} = 5$V and $V_{DS} = 2, 3, 4, 5$V (linear-scale). (b) $V_{DS} = 3$V and $V_{PG} = 3, 4, 5$V (linear-scale).

So to capture this behavior, we can define a modified current equation as follows:

$$I_{DS} = \left\{w\ I_{Eqn.(7)} + (1-w)\ I_{V_{DS} \approx 2V}\right\} \left(1 - e^{-\frac{V_{DS}{}^B}{A}}\right). \quad (15)$$

where, A and B were found to be functions of V_{GS} and V_{PG}. The equations employed for representing A and B are of the form:

$$A = s_0 + s_1 V_{GS} + s_2 V_{PG} + s_3 V_{PG}^2 + s_4 V_{GS} V_{PG} + s_5 V_{Gs}^2 + s_6 V_{GS}^3 + s_7 V_{GS} V_{PG}^2 + s_8 V_{GS}^2 V_{PG}, \quad (16)$$

$$B = t_0 + t_1 V_{PG} + t_2 V_{GS} + t_3 V_{GS} V_{PG} + t_4 V_{PG}^2. \quad (17)$$

Moreover:

$$w = \left\{\frac{1}{2} + \frac{1}{2}\ tanh\left(\frac{V_{DS} - 2V}{50mV}\right)\right\}, \quad (18)$$

was used to smoothly connect the "linear" and "saturation" regions.

Depicted in Fig. 10 are examples of the measured $I_{DS} - V_{DS}$ characteristics and their fitting using the

proposed model. Results are displayed in semi-logarithmic and linear scale showing good agreement in both cases.

Finally, Table 1 summarizes all the parameters used to fit the experimental data to the model.

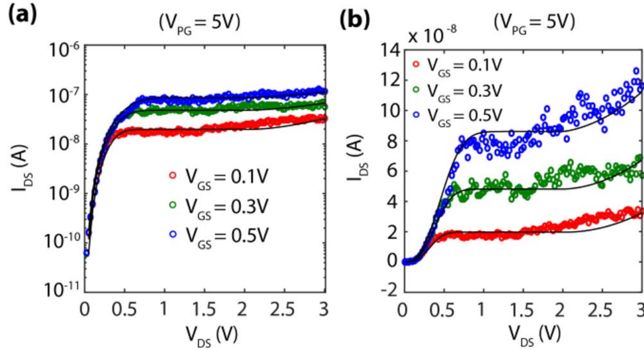

FIGURE 10. Experimental (circles) and modeled *I-V* characteristic for a DIG FinFET, with $V_{PG} = 5V$ and $V_{GS} = 0.1, 0.3, 0.5V$. (a) In semi-logarithmic scale. (b) In linear scale.

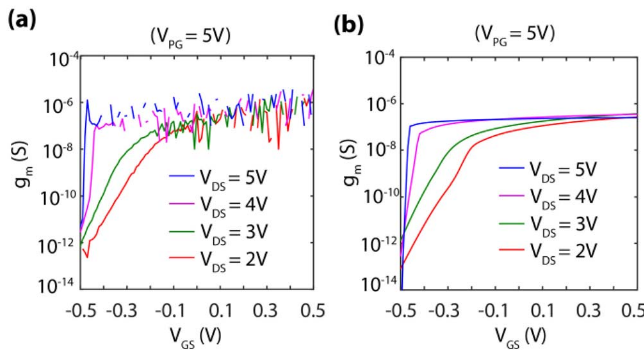

FIGURE 11. Transconductance (g_m): (a) directly extracted from the numerical derivative of the measured device data, and (b) evaluated from the model.

IV. PREDICTIVE NATURE

In order to evaluate the potential of electron devices for analog and RF applications, accurate estimates for the current-voltage characteristics as well as for its derivatives are required. For instance, compact models for TFETs enabled the evaluation of the perspectives of these devices for analog applications [13] as well as RF detectors [19]. In this regard, it is worth mentioning that numerical calculation of the derivatives directly from experimental device data can be prone to significant uncertainty when computing derivatives. From this point of view fitting of experimental data to a continuous compact model, whose derivatives are also continuous, can be therefore beneficial. Depicted in Fig. 11 is a typical plot of the trans-conductance (g_m) as directly extracted from the numerical derivative of the measured device data, and as evaluated from the model depicting this effect. From this point of view fitting of experimental data to a continuous compact model, whose derivatives are also continuous, can be therefore beneficial.

TABLE 1. Fitting parameters.

PARAMETER	PARAMETER VALUE	PARAMETER	PARAMETER VALUE
α_0	0.05507 V	r_0	-0.3548 V
β_0	2.348 x 10^{-8}	r_1	0.0783
γ_0	2..038 V^{-1}	r_2	0.3568
δ_0	2.092 V^{-1}	r_3	0.07945 V^{-1}
α_1	1.0 x 10^{-6}	r_4	-0.1935 V^{-1}
β_1	1.367 V^{-1}	r_5	-0.0317 V^{-1}
β_2	-0.04912 V^{-1}	r_6	-0.03445 V^{-2}
β_3	-0.1259 V^{-2}	r_7	0.0539 V^{-2}
β_4	-0.6986	r_8	-0.004 V^{-2}
p_0	-23.25	r_9	0.00285 V^{-2}
p_1	-45.02 V^{-1}	s_0	0.09588
p_2	75.4 V^{-1}	s_1	0.2357 V^{-1}
p_3	5.9 V^{-2}	s_2	-0.05913 V^{-1}
p_4	14.47 V^{-2}	s_3	0.009813 V^{-2}
p_5	-33.98 V^{-2}	s_4	-0.1246 V^{-2}
p_6	2.667 V^{-3}	s_5	-0.2963 V^{-2}
p_7	-6.18 V^{-3}	s_6	-0.3516 V^{-3}
p_8	1.96 V^{-3}	s_7	0.01688 V^{-3}
p_9	3.815 V^{-3}	s_8	0.2009 V
q_0	-1.115	t_0	3.276
q_1	0.8633 V^{-1}	t_1	0.1658 V^{-1}
q_2	0.5276 V^{-1}	t_2	-1.7 V^{-1}
q_3	-0.1 V^{-2}	t_3	0.2 V^{-2}
q_4	-0.01571 V^{-2}	t_4	-0.04583 V^{-2}
q_5	-0.06 V^{-2}		
μ_0	2.939 A		
μ_1	0.03424 A/V		
μ_2	3.86 x 10^{-5} A		
σ_0	0.8955 V^{-1}		
σ_1	1.076 V^{-1}		
σ_2	0.001335 V^{-2}		

In this section, we will discuss on the application of DIG-FinFETs as RF detectors at millimeter-wave and terahertz frequencies and predict the performance of these devices based on the developed model. Many detection approaches have been developed to-date [20], however, a miniaturized room-temperature detector technology, exhibiting a very sensitive broadband response at room-temperature, is still largely missing. Conventional FETs can operate as efficient detectors far beyond their fundamental cut-off frequency [21]. Indeed, FETs can intrinsically operate as non-resonant broadband detectors with high responsivity, because of self-mixing [22] as described by the Dyakonov-Shur theory [23].

When a RF field is applied between the gate and the source terminal of the transistor, this electric field is rectified, and a source-to-drain DC photo-current, or photo-voltage, dependent on the device configuration and boundary conditions, is induced. Assuming current detection and conjugate matching of an antenna coupling the incoming RF signal into the device so to provide maximum power transfer, the following upper bound for the detector responsivity can be obtained [24]–[26]:

$$R_i = \frac{1}{2\sigma_0}\frac{\partial \sigma_0}{\partial V_{GS}} = \frac{1}{2}\frac{\partial \ln I_{DS}(V_{GS})}{\partial V_{GS}} = \frac{1}{2}\frac{g_m}{I_{DS}}, \quad (19)$$

where σ_0 corresponds to the FET channel conductivity. Moreover, g_m in Eqn. (19) represents the transistor trans-conductance, and g_m/I_{DS} is the trans-conductance to

current ratio, which is an important factor, related to the slope in the current-voltage characteristics, and widely employed in analog circuit design. In traditional FETs, the g_m/I_{DS} ratio is theoretically limited to values below 38.5 V^{-1}, which sets a maximum attainable responsivity. The ratio between the responsivity in DIG FinFET detectors and the maximum attainable responsivity in traditional FETs is thus given by:

$$E = \frac{R_{i,\ DIG\ FinFET}}{R_{i,\max MOSFET}} = \frac{kT}{q}\frac{\partial \ln I_{DS}(V_{GS})}{\partial V_{GS}} = \frac{kT}{q}\frac{g_m}{I_{DS}}. \quad (20)$$

Plotted in Fig. 12 is the responsivity enhancement factor (E), as defined in Eqn. (20), for a DIG FinFET detector configuration where the polarity-gate voltage is set to $V_{PG} =$ 5V. E is plotted as a function of V_{GS} in order to depict the V_{GS} bias dependence of the response. Moreover, two cases are analyzed, corresponding to V_{DS} biases of: (i) $V_{DS} =$ 5V, where impact ionization is significant and the device shows maximum $SS << 60$ mV/dec, and (ii) $V_{DS} =$ 2V, where the SS is always > 60mV/dec. We observe that whereas in the first case, in the subthreshold region much larger responsivity than that in traditional FET detectors is attainable, in the second case, the responsivity is always smaller than the FET-limit. This is a result of the capability of attaining a smaller SS under large V_{PG} and V_{DS} biases because of impact ionization processes. In general, based on Eqns. (7) and (20), it is observed that:

$$E_{max} = \frac{R_{i,maxDIGFinFET}}{R_{i,\max MOSFET}} = \frac{kT}{q}\frac{2}{c_0}. \quad (21)$$

Therefore, the smallest c_0, the largest the detector responsivity. As a general rule, c_0 will benefit from: (a) large applied voltages (V_{PG} and V_{DS}), thus large slopes in the electric field, (b) small polarity-gate lengths, and (c) from the incorporation of direct-gap materials with smaller bandgap than that of Si at the drain-end of the device so to boost carrier multiplication processes as carriers drift from the control-gate-controlled channel to the drain contact.

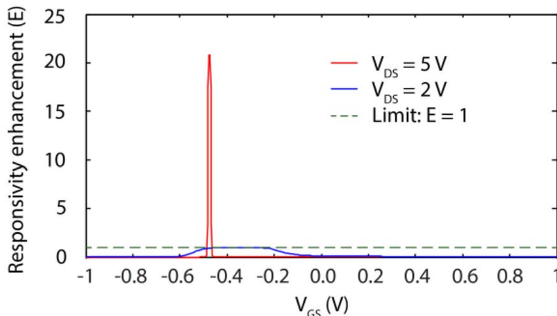

FIGURE 12. **Estimated current-responsivity enhancement (*E*) as a function of V_{GS} bias for two different drain biases for a DIG FinFET configured as RF detector ($V_{PG} =$ 5V). The RF responsivity is estimated from the developed DC compact model of the device.**

V. CONCLUSION

We discussed an analytic DIG FinFET continuous compact model capable of capturing the current–voltage characteristics of the DIG FinFET in all the device operation regions. Although our discussion is focused only with regards to n-type operation, the model can be readily adapted to also describe the p-type operation. The model accounts for the bias-dependent super steep subthreshold swing, leakage levels, as well as the above-threshold characteristics of the device. To prove the validity of the model, the model was fitted to experimental results on fabricated devices. An excellent agreement was observed. Moreover, based on the proposed model, we predict on the performance of DIG FinFETs as RF detectors.

REFERENCES

[1] Q. Zhang, W. Zhao, and A. Seabaugh, "Low-subthreshold-swing tunnel transistors," *IEEE Electron Device Lett.*, vol. 27, no. 4, pp. 297–300, Apr. 2006.

[2] A. C. Seabaugh and Q. Zhang, "Low-voltage tunnel transistors for beyond CMOS logic," *Proc. IEEE*, vol. 98, no. 12, pp. 2095–2110, Dec. 2010.

[3] A. M. Ionescu and H. Riel, "Tunnel field-effect transistors as energy-efficient electronic switches," *Nature*, vol. 479, no. 7373, pp. 329–337, 2011.

[4] D. Sarkar *et al.*, "A subthermionic tunnel field-effect transistor with an atomically thin channel," *Nature*, vol. 526, no. 7571, pp. 91–95, 2015.

[5] L. Liu, D. Mohata, and S. Datta, "Scaling length theory of double-gate interband tunnel field-effect transistors," *IEEE Trans. Electron Devices*, vol. 59, no. 4, pp. 902–908, Apr. 2012.

[6] J. Zhang, M. De Marchi, P.-E. Gaillardon, and G. De Micheli, "A Schottky-barrier silicon FinFET with 6.0 mV/dec subthreshold slope over 5 decades of current," in *IEDM Tech. Dig.*, San Francisco, CA, USA, 2014, pp. 13.4.1–13.4.4.

[7] J. Zhang, J. Trommer, W. M. Weber, P.-E. Gaillardon, and G. D. Micheli, "On temperature dependency of steep subthreshold slope in dual-independent-gate FinFET," *IEEE J. Electron Devices Soc.*, vol. 3, no. 6, pp. 452–456, Nov. 2015.

[8] J. G. Fossum, R. Sundaresan, and M. Matloubian, "Anomalous subthreshold current–voltage characteristics of n-channel SOI MOSFET's," *IEEE Electron Device Lett.*, vol. 8, no. 11, pp. 544–546, Nov. 1987.

[9] Z. Lu *et al.*, "Realizing super-steep subthreshold slope with conventional FDSOI CMOS at low-bias voltages," in *IEDM Tech. Dig.*, San Francisco, CA, USA, 2010, pp. 16.6.1–16.6.3.

[10] P.-E. Gaillardon, J. Zhang, M. De Marchi, and G. De Micheli, "Towards functionality-enhanced devices: Controlling the modes of operation in three-independent-gate transistors," in *Proc. 10th IEEE Nanotechnol. Mater. Devices Conf. (NMDC)*, Anchorage, AK, USA, 2015, pp. 1–2.

[11] H. Lu, D. Esseni, and A. Seabaugh, "Universal analytic model for tunnel FET circuit simulation," *Solid State Electron.*, vol. 108, no. 1, pp. 110–117, Jun. 2015.

[12] H. Lu, J. W. Kim, D. Esseni, and A. Seabaugh, "Continuous semiempirical model for the current–voltage characteristics of tunnel FETs," in *Proc. 15th Int. Conf. Ultimate Integr. Silicon (ULIS)*, Stockholm, Sweden, 2014, pp. 25–28.

[13] L. Barboni, M. Siniscalchi, and B. Sensale-Rodriguez, "TFET-based circuit design using the transconductance generation efficiency g_m/I_d method," *IEEE J. Electron Devices Soc.*, vol. 3, no. 3, pp. 208–216, May 2015.

[14] J. Wu and Y. Taur, "A continuous semianalytic current model for DG and NW TFETs," *IEEE Trans. Electron Devices*, vol. 63, no. 2, pp. 841–847, Feb. 2016.

[15] Y. Dong, L. Zhang, X. Li, X. Lin, and M. Chan, "A compact model for double-gate heterojunction tunnel FETs," *IEEE Trans. Electron Devices*, vol. 63, no. 11, pp. 4506–4513, Nov. 2016.

[16] J. Wu, J. Min, and Y. Taur, "Short-channel effects in tunnel FETs," *IEEE Trans. Electron Devices*, vol. 62, no. 9, pp. 3019–3024, Sep. 2015.

[17] J. H. Mathews and K. D. Fink, "Curve fitting," in *Numerical Methods Using MATLAB*, 4th ed. Upper Saddle River, NJ, USA: Prentice-Hall, 2004, ch. 5, sec. 5. 2, pp. 263–275.

[18] A. Keshavarzi, K. Roy, and C. F. Hawkins, "Intrinsic leakage in low power deep submicron CMOS ICs," in *Proc. Int. Test Conf.*, Washington, DC, USA, 1997, pp. 146–155.
[19] W. Li, T. Yu, J. Hoyt, and P. Fay, "InGaAs/GaAsSb interband tunneling FETs as tunable RF detectors," in *Proc. Device Res. Conf. (DRC)*, Santa Barbara, CA, USA, 2014, pp. 21–22.
[20] A. Rogalski and F. Sizov, "Terahertz detectors and focal plane arrays," *Opto Electron. Rev.*, vol. 19, no. 3, pp. 346–404, 2011.
[21] W. Knap *et al.*, "Field effect transistors for terahertz detection: Physics and first imaging applications," *J. Infrared Millim. Terahertz Waves*, vol. 30, no. 12, pp. 1319–1337, 2009.
[22] A. Lisauskas *et al.*, "Rational design of high-responsivity detectors of terahertz radiation based on distributed self-mixing in silicon field-effect transistors," *J. Appl. Phys.*, vol. 105, no. 11, 2009, Art. no. 114511.
[23] M. Dyakonov and M. Shur, "Detection, mixing, and frequency multiplication of terahertz radiation by two-dimensional electronic fluid," *IEEE Trans. Electron Devices*, vol. 43, no. 3, pp. 380–387, Mar. 2006.
[24] A. Lisauskas *et al.*, "Terahertz detection with field-effect transistors: Intrinsic versus device sensitivity limits," in *Proc. Opt. Sensors*, Barcelona, Spain, 2014, Art. no. SeTu5A-2.
[25] P. Földesy, "Terahertz responsivity of field-effect transistors under arbitrary biasing conditions," *J. Appl. Phys.*, vol. 114, no. 11, 2013, Art. no. 114501.
[26] M. Sakowicz *et al.*, "Terahertz responsivity of field effect transistors versus their static channel conductivity and loading effects," *J. Appl. Phys.*, vol. 110, no. 5, 2011, Art. no. 054512.

MEHDI HASAN received the B.S. degree in electrical and electronic engineering from the Bangladesh University of Engineering and Technology, Dhaka, Bangladesh, in 2009, and the M.S. degree in electrical and computer engineering from the University of New Mexico, Albuquerque, NM, USA, in 2012. He is currently pursuing the Ph.D. degree in electrical and computer engineering with the University of Utah, Salt Lake City, UT, USA.

PIERRE-EMMANUEL GAILLARDON (S'10–M'11) received the Electrical Engineer degree from CPE-Lyon, France, in 2008, the M.Sc. degree in electrical engineering from INSA Lyon, France, in 2008, and the Ph.D. degree in electrical engineering from CEA-LETI, Grenoble, France, and the University of Lyon, France, in 2011. He was a Research Associate with the Swiss Federal Institute of Technology (EPFL), Lausanne, Switzerland, within the Laboratory of Integrated Systems (Prof. De Micheli) and a Visiting Research Associate with Stanford University, Palo Alto, CA, USA. He is an Assistant Professor with the Electrical and Computer Engineering Department, University of Utah, Salt Lake City, UT, USA, where he leads the Laboratory for NanoIntegrated Systems. Previously, he was research assistant at CEA-LETI, Grenoble, France. His research activities and interests are currently focused on the development of reconfigurable logic architectures and digital circuits exploiting emerging device technologies and novel EDA techniques. He was a recipient of the C-Innov 2011 Best Thesis Award and the Nanoarch 2012 Best Paper Award. He is an Associate Editor of the IEEE TRANSACTIONS ON NANOTECHNOLOGY. He has been serving as a TPC Member for many conferences, including DATE'15–16, DAC'16, Nanoarch'12–16. He is a Reviewer for several journals and funding agencies.

BERARDI SENSALE-RODRIGUEZ (S'07–M'13) received the Engineer's degree from the Universidad de la República, Uruguay, in 2008, and the Ph.D. degree from the University of Notre Dame in 2013. In 2013, he joined the faculty of the University of Utah, where he is currently an Assistant Professor of electrical and computer engineering. His early research interests were focused on numerical modeling of RF/microwave components and analog circuit design oriented toward low power (sub-threshold) portable and implantable electronics. His doctoral work was focused on the proposal and development of novel THz devices and systems. More recent interests include plasmonics, metamaterials, and optoelectronic devices. He has authored/co-authored over 70 research articles in the above areas. He was a recipient of the Best Student Paper Award at the 37th International Conference on Infrared, Millimeter and Terahertz Waves, the First Prize in the Engineering Division of Notre Dame's 2013 Graduate Research Symposium, the Eli J. and Helen Shaheen Award in Engineering (Highest Honor Bestowed on Notre Dame Graduate Students), and the NSF CAREER Award. He is an Associate Member of the Uruguayan National Researchers System (SNI). He is a member of Tau Beta Pi and APS.